Observations of the nightside ionosphere of Mars by the Mars Express Radio Science Experiment (MaRS)

Paul Withers,[1] M. O. Fillingim,[2] R. J. Lillis,[2] B. Häusler,[3] D. P. Hinson,[4] G. L. Tyler,[4] M. Pätzold,[5] K. Peter,[5] S. Tellmann,[5] and O. Witasse[6]

[1] The vertical structure of the nightside ionosphere of Mars and its dependence on solar zenith angle are currently poorly determined, as is the importance of two key sources of nightside plasma, electron precipitation and transport of dayside plasma. We examined 37 electron density profiles of the ionosphere of Mars at solar zenith angles of 101°–123° obtained by the Mars Express Radio Science Experiment (MaRS) between 18 August and 1 October 2005. In general, solar activity was low during this period, although several solar energetic particle events did occur. The results show that (1) trends in peak electron density and altitude with solar zenith angle are consistent with transport of dayside plasma as an important plasma source up to 115°, but not higher; (2) peak altitudes of around 150 km observed at larger (>115°) solar zenith angles are consistent with simulated plasma production by electron precipitation; and (3) peak altitudes observed during solar energetic particle events are at 90 km, consistent with accepted models. Solar energetic particle events can be the main source of nightside plasma. These results challenge current models of the nightside ionosphere, including their implications for plasma sources. The total electron content is correlated with peak electron density, requiring explanation. Due to the geographical distribution of this data set (latitudes poleward of 38°N), we do not explore the influence of crustal field strength and direction on the nightside ionosphere.

1. Introduction

[2] The nightside ionosphere is an important feature of the atmosphere and space environment of Mars. It participates in the global-scale plasma circulation and system of electromagnetic fields and currents, and is a conduit through which the energy and momentum of particles in the space environment are transferred into the neutral atmosphere, a lower boundary for the magnetosphere, and a reservoir from which volatile species are removed from Mars. Its vertical and horizontal structure, chemical composition, dynamics, thermal state, and electrodynamics currently are poorly constrained by observations, although the nightside ionosphere is clearly affected by local magnetic field conditions. Here we report results from occultation observations of the nightside ionosphere of Mars by the Mars Express (MEX) Radio Science Experiment MaRS: we explore and interpret the vertical structure, and address the degree to which peak altitudes, densities, and shapes are consistent with theoretical predictions.

2. Previous Observations of the Nightside Ionosphere

[3] The main instruments used to study the ionosphere of Mars have been the Viking Lander (VL) Retarding Potential Analyzers (RPAs) [*Hanson et al.*, 1977], the MARSIS radar sounder on MEX [*Gurnett et al.*, 2008], and radio occultation investigations on Mariner 9 (M9) [*Kliore et al.*, 1972, 1973], the two Viking Orbiters [*Lindal et al.*, 1979], Mars Global Surveyor (MGS) [*Hinson et al.*, 1999; *Withers et al.*, 2008], MEX [*Pätzold et al.*, 2005], as well as earlier flyby spacecraft [*Mendillo et al.*, 2003]. Of these, the only data that cover solar zenith angles (SZAs) greater than 90°, above which the planet's surface is shadowed from solar radiation, are from MARSIS and occultations by Mars 4 and 5, Viking Orbiters 1 and 2, and MEX MaRS. Yet darkness does not

[1]Astronomy Department, Boston University, Boston, Massachusetts, USA.

[2]Space Sciences Laboratory, University of California, Berkeley, California, USA.

[3]Institut für Raumfahrttechnik, Universität der Bundeswehr München, Munich, Germany.

[4]Department for Electrical Engineering, Stanford University, Stanford, California, USA.

[5]Rheinisches Institut für Umweltforschung, Abteilung Planetenforschung, Universität zu Köln, Cologne, Germany.

[6]ESA-ESTEC, Noordwijk, Netherlands.

Corresponding author: P. Withers, Astronomy Department, Boston University, 725 Commonwealth Ave., Boston, MA 02215, USA. (withers@bu.edu)
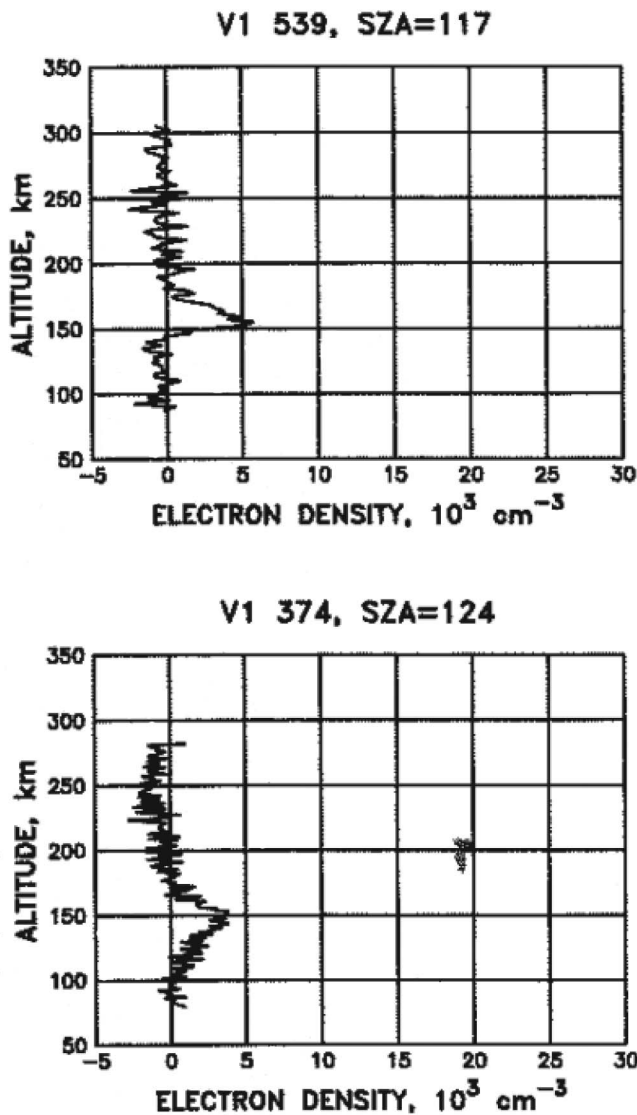
V1 539, SZA=117

V1 374, SZA=124

Figure 1. Two profiles of electron densities in the dark ionosphere from Viking 1 radio occultation. (top) The ingress occultation from orbit 539 at SZA = 117°, latitude 39.65°N, and longitude 186.85°W. (bottom) The ingress occultation from orbit 374 at SZA = 124°, latitude 23.45°N, and longitude 79.69°W. The shapes, peak densities, and peak altitudes of these profiles can be compared to predictions and Mars Express observations. Reproduced from *Zhang et al.* [1990, Figure 1a].

engulf the atmosphere precisely at an SZA of 90°, when the sun sets at the solid surface of a spherical planet. Instead, the atmosphere remains illuminated until greater SZAs. On Mars, the sun does not set at a representative ionospheric altitude of 120 km altitude until SZA = 105°. We distinguish between the twilight or near-terminator ionosphere (90° < SZA < 105°) and the dark ionosphere (SZA > 105°). Much previous work on the nightside ionosphere (SZA > 90°) addresses the twilight ionosphere, but not the dark ionosphere.

[4] We first consider measurements of the vertical structure of the dark ionosphere. The primary interpretation of the vertical structure of the nightside ionosphere of Mars is that of *Zhang et al.* [1990], who analyzed 50 electron density profiles from Viking to explore the vertical structure of the nightside ionosphere at SZAs of 90°–125°; measurable quantities of plasma were present in only 19 of these profiles. The smallest reported peak density, which should indicate the detection threshold of the instrument, was ∼5 × 10^3 cm^{-3}. *Zhang et al.* [1990, Figure 3] show that the probability of detecting the ionosphere was >80% at SZA = 90°–100°, but <50% at SZA = 100°–125°. Hence, at SZA > 100°, ionospheric densities fluctuate around the detection limit due to some combination of spatial and temporal variations,. We note that some recent workers [*Lillis et al.*, 2009; *Withers*, 2009; *Němec et al.*, 2011] have misinterpreted an ambiguous sentence of *Zhang et al.* [1990] and stated that the *average* peak density was ∼5 × 10^3 cm^{-3}. Inspection of *Zhang et al.* [1990, Figure 3] shows this to be incorrect.

[5] Very few electron density profiles from Mars with SZA > 90° have been published: two are shown by *Savich and Samovol* [1976] (and also are given by *Vasil'ev et al.* [1975] and *Moroz* [1976]), three are shown by *Zhang et al.* [1990, Figure 1a] (one of which is also shown by *Lindal et al.* [1979, Figure 8]), and about a dozen are given by *Kliore* [1992].

[6] In only four of the above examples is the ionosphere fully shadowed from sunlight, which requires SZA > 105°. As a result, most of the published "nightside" profiles are more accurately described as twilight profiles that located above the shadow of Mars and are hence sunlit to some extent. Several workers have used profiles at SZA = 90°–100° to infer a typical peak altitude of 150–180 km for "the nightside ionosphere," which is not strictly accurate [*Withers*, 2009; *Němec et al.*, 2011]. Rather, these peak altitudes of 150–180 km are precisely those expected as a result of the rise in the altitude of the dayside M2 layer with increasing SZA [*Hantsch and Bauer*, 1990; *Zhang et al.*, 1990].

[7] The behavior of the dark ionosphere is different from the behavior of the twilight ionosphere. The handful of peak altitudes reported by *Zhang et al.* [1990] with SZAs beyond 105° are scattered between 135 km and 170 km, with lower altitudes and greater plasma densities than expected for photoionization at the stated SZAs. Instead, such plasma must be either (1) transported into the dark ionosphere from the dayside or (2) produced in situ by electron precipitation.

[8] The Mars 4 egress profile [*Moroz* 1976, Figure 3] probed the dark ionosphere at SZA = 127°: the peak density is 4.6 × 10^3 cm^{-3}, peak altitude 110 km, full width at half maximum (FWHM) 50 km, and the asymmetric shape is reminiscent of a dayside Chapman layer. The Mars 5 egress profile at SZA = 106° is similar [*Savich and Samovol*, 1976]. Figure 1 shows two profiles of the dark ionosphere from Viking Orbiter 1. The upper profile (SZA = 117°) has a peak density of 5 × 10^3 cm^{-3}, a peak altitude of 150 km, a FWHM of 20 km, and an asymmetric shape also reminiscent of a dayside Chapman layer. The lower profile (SZA = 124°) has a peak density of 4 × 10^3 cm^{-3}, a peak altitude of 150 km, a FWHM of 30–40 km, and an asymmetric shape. For this asymmetric profile, the strongest gradient is found above the main ionospheric peak. By contrast, the strongest gradients in the asymmetric shapes of dayside
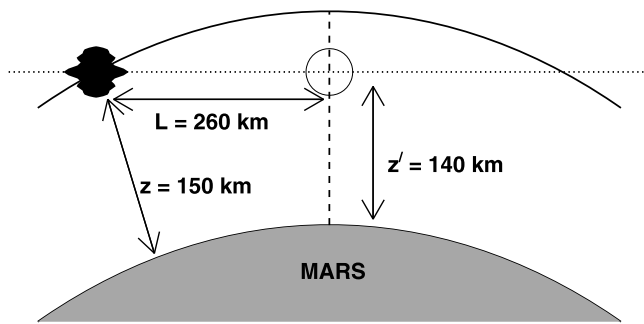
Figure 2. Illustration of how horizontal inhomogeneities in the distribution of plasma affect derived electron density profiles. Here a radio occultation experiment sounds the ionosphere of Mars, with the radio ray at this particular instant shown by the horizontal dotted line. The spacecraft and ground station are beyond the left and right of this image. The irregular solid shape represents a blob of plasma at 150 km altitude. The point of closest approach of the radio ray to the center of Mars is marked by the vertical dashed line. The intersection of the dotted and dashed lines, marked by the open disk, is the apparent location of the blob of plasma at the lower altitude of 140 km.

ionospheric profiles, the upper Viking Orbiter profile in Figure 1 (dark), and the Mars 4 egress profile (dark) are found below the main ionospheric peak.

[9] We turn now from measurements of the vertical structure of the dark ionosphere to more numerous measurements of the peak electron density of the dark ionosphere. The MARSIS radar sounder can measure the ionospheric peak electron density at solar zenith angles greater than 90° with a detection limit of 5×10^3 cm^{-3} [Gurnett et al., 2008; Němec et al., 2010]. Gurnett et al. [2008] reported that detections of ionospheric plasma at 90° < SZA < 110° were often localized, peak densities were highly variable, and the nature of the corresponding radar echoes was consistent with a high degree of horizontal structure. They confirmed that the nightside ionosphere at a single time is patchy, indicating the importance of spatial variability. Němec et al. [2010] found that the probability of the peak density in the dark ionosphere exceeding the MARSIS detection limit decreased with increasing SZA from 107° until 125°, where it reached a stable floor; they concluded from this observation that the transport of dayside plasma is an important source of nightside plasma for SZA < 125°. Němec et al. [2010] also found that in regions of strong crustal field SZA was not an important controlling factor for the likelihood of detecting plasma in the dark ionosphere. Instead, the detection probability was four times higher in regions of near-vertical field than in regions of near-horizontal field, which implies that here ionization by precipitating electrons is the dominant source of plasma. Němec et al. [2011] found that regions of strong vertical magnetic field, where the field lines are open to the space environment, can exhibit substantial plasma densities (>5 × 10^4 cm^{-3}) at SZA > 125°. These large densities imply a plasma production rate of 500 cm^{-3} s^{-1}, assuming O_2^+ ions and a dissociative recombination coefficient of 2×10^{-7} cm^3 s^{-1} [Schunk and Nagy, 2009; Mendillo et al., 2011; Lollo et al., 2012].

[10] Finally, we turn to measurements of the total electron content (TEC) of the dark ionosphere. Lillis et al. [2010], using MARSIS TEC measurements, observed temporal variations in TEC at 90° < SZA < 130° that were the result of solar activity. Some solar energetic particle events were found to double TEC. The importance of vertical magnetic fields for MARSIS TEC measurements was also shown by Safaeinili et al. [2007].

[11] Duru et al. [2011] studied the nightside ionosphere of Mars above 350 km using MARSIS measurements of local electron density at the spacecraft, but this altitude range is far above that addressed here.

3. Spherical Symmetry and Occultation Observations

[12] One critical factor intrinsic to radio occultation measurements must be discussed before going further. The data processing technique can only uniquely constrain changes in the properties of the refractive medium (the ionosphere and neutral atmosphere) in one dimension, not all three dimensions [Fjeldbo et al., 1971]. Changes in the other dimensions must be specified a priori. The most common assumption is that there are no changes in neutral and ionospheric density along equipotential surfaces. If these surfaces are spherical, then the atmosphere and ionosphere are assumed to be spherically symmetric. That is, there are no circumferential (horizontal) gradients in the atmosphere or ionosphere.

[13] Clearly, this assumption need not be satisfied in regions distant from those probed by the radio signal. It is not trivial to determine the critical lateral extent over which this assumption must be satisfied. For radio occultation measurements of the neutral atmosphere, basic principles require that the dependence of density on altitude can be well approximated by an exponential decrease over a wide range of vertical distances. In this instance, the assumption of spherical symmetry (or equivalent) must be satisfied over a horizontal distance of about $2L = 2\sqrt{2RH}$, where R is taken as the radius of closest approach of the occultation ray (often approximated as the planetary radius, 3400 km for Mars) and H is the neutral scale height [Hinson et al., 1999]. For $H = 10$ km, $L = 260$ km. If the spatial distribution of the particles responsible for refraction of radio waves does not depend exponentially on altitude, then the expression for the critical horizontal distance is different [Lipa and Tyler, 1979]. The vertical structure of the nightside ionosphere is poorly known, spatially variable, and temporally variable, which prevents us from calculating a more appropriate expression for the critical horizontal distance.

[14] Figure 2 illustrates how lateral inhomogeneities in the spatial distribution of plasma affect derived electron density profiles. Figure 2 schematically represents one instant at which a radio occultation experiment sounds the ionosphere of Mars, emphasizing the path of the radio ray at this particular instant and the occultation point, which is the radio ray's point of closest approach to the center of Mars (140 km altitude). Some distance away from the occultation point, a blob of plasma is encountered by this radio ray at a higher altitude. If the blob of plasma is 260 km away from the occultation point, then trigonometric analysis shows its altitude is 150 km. When the data are processed, the effects

of this blob of plasma at 150 km are erroneously distributed by the inversion algorithm to all altitudes below 140 km.

[15] Despite the absence of a priori knowledge concerning the vertical and horizontal structure of the nightside ionosphere, we can make some general comments on the effects of inhomogeneities on the resulting ionospheric profiles.

[16] 1. If a localized region of high-density plasma some horizontal distance away from the occultation point, as in Figure 2, is responsible for the presence of a plasma layer in the derived density profile inferred under the assumption of spherical symmetry, then the altitude of the layer in the derived density profile is at or below the true altitude of this localized region of high-density plasma.

[17] 2. The density of the plasma in the derived layer underestimates the true density of this localized region of high-density plasma.

[18] 3. Strong vertical gradients in a derived electron density profile (see, for example, the plasma layer at 90 km in profile C3 in Figure 3c) are hard to attribute to a non-spherically symmetric distribution of plasma. If a spherically symmetric distribution of plasma contains a strong vertical gradient, then the derived electron density profile will also include a strong vertical gradient. For a nonspherically symmetric distribution of plasma to cause a strong vertical gradient in a derived electron density profile requires a strong vertical gradient and a strong horizontal gradient in the plasma distribution. Atypical ionospheric conditions are required to maintain strong gradients in both directions, and so our preferred explanation for strong vertical gradients in derived electron density profiles is strong vertical gradients in a spherically symmetric ionosphere.

4. Previous Simulations of the Nightside Ionosphere

[19] Two sources of plasma, ionization by precipitating electrons and transport of dayside plasma, are generally thought to be the most important sources of nightside plasma [Fox et al., 1993]. Several groups have used numerical simulations to study the effects of precipitating electrons on the nightside ionosphere [Haider et al., 1992; Fox et al., 1993; Lillis et al., 2009, 2011; Fillingim et al., 2010]. Related work was carried out by Bertaux et al. [2005], who examined the production of auroral emissions by precipitating electrons. Fox et al. [1993], who also included the transport of dayside plasma as a source of nightside plasma by imposing an ad hoc downward flux of plasma at the upper boundary of the model found that these two sources of plasma, ionization by precipitating electrons and transport of dayside plasma, contributed equally to the peak electron density.

[20] Haider et al. [1992] and Fox et al. [1993] predicted peak electron densities of 10^4 cm^{-3} based on a small number of possible electron spectra derived from Phobos 2 measurements. Fillingim et al. [2010] used a wide range of possible electron energy spectra and pitch angle distributions based upon MGS electron reflectometer measurements to predict peak electron densities between 10^2 and 3×10^4 cm^{-3}. Lillis et al. [2009, 2011] used the same source of electron spectra as Fillingim et al. [2010], but included the focusing effects of crustal fields, to predict a range of peak densities similar to that of to Fillingim et al. [2010]. Small peak

densities of Lillis et al. [2009, 2011] and Fillingim et al. [2010] were associated with "plasma voids", regions where strong horizontal fields shield the atmosphere from impinging electrons. Large peak densities were associated with magnetic cusps, localized open field regions that produce magnetic focusing of incident electron fluxes.

[21] The above range of peak density predictions is generally consistent with the observations described in section 2, although all these predictions fall below the large plasma densities ($>5 \times 10^4$ cm^{-3}) reported by Němec et al. [2011] for regions of strong vertical crustal field. Haider et al. [1992] predicted peak altitudes of 140–160 km, Fox et al. [1993] 160–180 km, Fillingim et al. [2010] 100–160 km, and Lillis et al. [2009, 2011] 120–180 km. These predictions are broadly consistent with 135–170 km range found in observations at SZA > 100° by Zhang et al. [1990], with the exception of the lower part of the range predicted by Fillingim et al. [2010].

[22] The low peak altitudes predicted by Fillingim et al. [2010] occurred for two distinct cases: (1) in plasma voids where peak densities approach 100 cm^{-3}, which is below the detection limits of radio occultations and MARSIS, and (2) in a few instances given by Fillingim et al. [2010, Figure 2] outside plasma voids where peak densities are 10^4 cm^{-3}; the most striking example can be seen at 39°S of Fillingim et al. [2010, Figure 2]. The high densities at low altitudes are associated with electron fluxes at 10 keV and greater that slightly exceed the instrumental background, in contrast to typical instances when these high-energy fluxes hover at the instrumental background. Due to the influence of the instrumental background, we view this aspect of the results of Fillingim et al. [2010] with caution.

[23] Fox et al. [1993] predicted smooth, relatively symmetric profile shapes in contrast to the observations summarized here in section 2. Haider et al. [1992], on the other hand, predicted a smooth shape that was more asymmetric with the largest gradient on the bottomside. Similarly, most of the profile shapes predicted by Lillis et al. [2011] are smooth and asymmetric with the largest gradient on the bottomside, but some examples (e.g., profiles 4 and 5 in Lillis et al. [2011, Figure 5]) display a more complex vertical structure associated with electron energy distributions that are close to the instrumental background at keV energies. Also, these two electron energy distributions are relatively flat. That is, fluxes at keV energies are not much smaller than fluxes at energies of hundreds of eV.

[24] Simulated peak densities, altitudes, and shapes seen in these models are generally consistent with observations and spatial variations in the precipitating electron population appear sufficient to account for observed ionospheric patchiness.

5. Mars Express Observations

[25] The MEX Radio Science Experiment (MaRS) team [Pätzold et al., 2004, 2005, 2009] has processed 557 vertical profiles of ionospheric electron density from the period 3 April 2004 to 7 August 2011. Of these 149 have SZA > 90° and 76 have SZA > 100°. Orbital geometry prevents radio occultations of Mars from probing the deep nightside of the planet; the greatest SZA observed by MEX to date is 128°, which is close to the geometric limit.
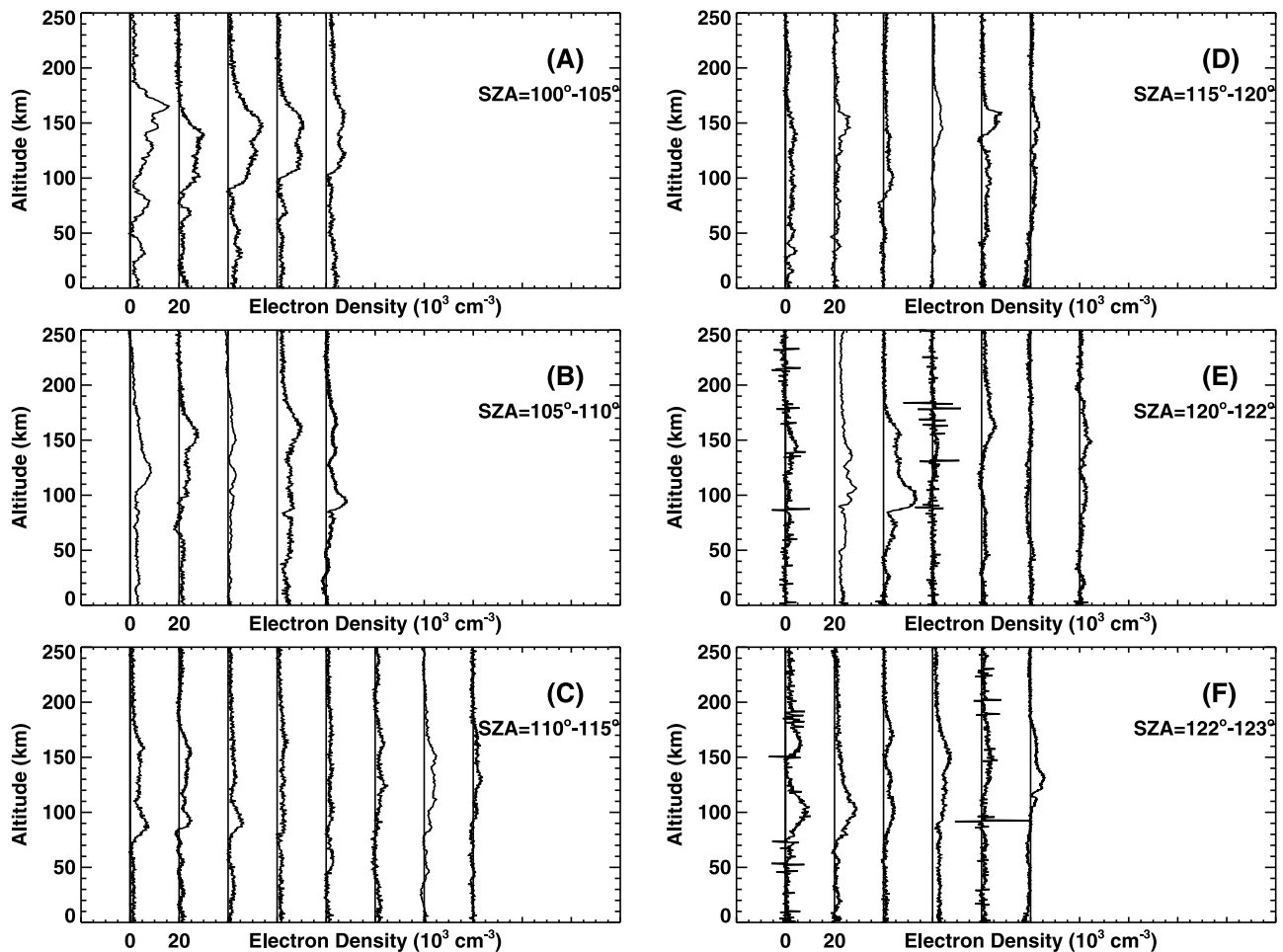
Figure 3. MEX MaRS electron density profiles. The horizontal axis is linear. Each profile in Figures 3a–3f is offset from its neighbor by 2×10^4 cm^{-3}. Vertical lines indicate zero electron density for each profile. Time, location, and other relevant information for each profile are given in Table 1. Leftmost profile in Figure 3a is profile A1, etc. The SZA range included is as shown. Note that an altitude of 120 km is illuminated by sunlight for SZA $\leq 105°$.

[26] We focus on a set of 37 profiles obtained by the two-way differential Doppler technique [*Pätzold et al.*, 2004] between 18 August and 1 October 2005 (days of year 230–274, orbits 2045–2204) for which the solar zenith angles are 101°–123°. Observation times, locations, and other relevant information for each profile are listed in Table 1. As they illustrate twilight conditions, we include the profiles at 101°–105° in our discussion, although they do not satisfy our definition of the dark ionosphere (SZA > 105°).

[27] The above set of profiles is distinguished by its very high data quality. We assume that the uncertainty in the each electron density measurement from a single occultation is constant. We adopt the standard deviation of electron densities between 500 km and 700 km altitude in a given profile as the 1σ uncertainty for all electron densities in that profile. These values are listed in Table 1 as the uncertainties in the peak electron densities. The root-mean-square value of the 37 uncertainties is 700 cm^{-3}. Note that all profiles are north of 38°N, remotely situated from the crustal magnetic field regions, and have crustal field strengths of <30 nT at 150 km altitude [*Arkani-Hamed*, 2004].

[28] These profiles are shown in Figure 3. We label the leftmost profile in Figure 3a as profile A1, etc. Some of the profiles (E1, E4, F1, and F5) contain occasional spikes, which are attributed to "cycle slips" in the receiver at the ESA New Norcia ground station in Australia, a sporadic technical problem that persisted in the receiver for several weeks. (We identified a spike as any electron density measurement that differs substantially from those immediately above and below it. True variations in ionospheric electron density with altitude persist for more than a single data point. We ignore such spikes in subsequent discussions.)

[29] The profiles extend to altitudes well above the 250 km altitude at which Figures 3 is truncated. Data from much higher altitudes were used to calculate the baseline for each electron density profile. Hence the positive electron densities occasionally present at 250 km in Figures 3a–3c may be accurate measurements, rather than indications of errors in the baseline. The relatively rare occurrence of nonzero electron densities at 250 km in Figures 3d–3f can therefore be interpreted as the absence of high-altitude plasma at SZA > 115° relative to SZA < 115°.

Table 1. Time, Location, and Other Relevant Information for Each Profile in Figure 3[a]

Profile	SZA (deg)	DOY	Orbit	Lat (°N)	Lon (°E)	$|B_{150}|$ (nT)	Inc (deg)	N_m (10^3 cm^{-3})	z_m (km)	TEC (10^{10} cm^{-2})
A1	101.1	230	2045	74	11	27	10	15.9 ± 0.8	165^{+1}_{-1}	9.2
A2	101.4	230	2046	75	274	5	54	10.5 ± 0.6	139^{+1}_{-1}	4.5
A3	101.8	230	2047	75	177	16	27	14.4 ± 0.6	147^{+1}_{-1}	9.5
A4	103.8	232	2054	76	220	14	78	11.1 ± 0.5	145^{+1}_{-1}	7.0
A5	104.6	233	2057	76	290	7	69	8.3 ± 0.6	123^{+1}_{-1}	6.8
B1	105.2	234	2059	76	96	6	47	8.6 ± 0.4	120^{+1}_{-1}	5.6
B2	105.8	234	2061	76	263	8	69	8.1 ± 0.5	153^{+1}_{-1}	3.5
B3	106.3	235	2063	76	70	19	47	3.3 ± 0.3	150^{+1}_{-1}	1.8
B4	106.9	236	2065	76	237	5	12	10.4 ± 0.7	163^{+1}_{-1}	8.4
B5	109.9	239	2076	75	254	5	23	8.8 ± 0.5	94^{+1}_{-1}	4.2
C1	110.7	239	2079	74	323	7	68	7.7 ± 0.5	87^{+1}_{-1}	5.0
C2	111.0	240	2080	74	226	9	11	5.5 ± 0.7	93^{+1}_{-1}	2.8
C3	111.5	240	2082	74	32	22	6	6.2 ± 0.5	90^{+1}_{-2}	3.5
C4	112.5	241	2086	73	4	13	40	4.5 ± 0.5	163^{+1}_{-1}	3.5
C5	113.2	242	2089	72	72	6	37	3.4 ± 0.4	100^{+1}_{-1}	2.6
C6	114.2	243	2093	71	43	9	30	5.4 ± 0.8	124^{+1}_{-1}	2.4
C7	114.7	244	2095	70	208	10	11	5.0 ± 0.9	151^{+4}_{-2}	3.1
C8	114.9	244	2096	70	111	3	26	3.9 ± 0.6	132^{+1}_{-1}	1.0
D1	115.1	245	2097	70	13	10	27	4.8 ± 0.6	140^{+1}_{-1}	3.1
D2	115.3	245	2098	69	276	1	23	6.3 ± 0.9	146^{+1}_{-1}	2.5
D3	117.3	247	2107	66	117	5	40	4.2 ± 0.5	103^{+1}_{-1}	2.1
D4	117.7	248	2109	66	282	3	24	4.1 ± 0.3	145^{+2}_{-3}	2.1
D5	118.0	248	2111	65	86	9	37	8.3 ± 0.5	159^{+1}_{-1}	3.1
D6	119.0	274	2204	38	54	20	9	3.8 ± 0.5	146^{+1}_{-1}	2.0
E1	120.3	252	2125	60	156	8	1	4.5 ± 1.1	145^{+7}_{-5}	1.5
E2	120.5	253	2126	60	58	3	12	8.9 ± 0.5	106^{+1}_{-1}	7.4
E3	121.9	256	2139	55	223	19	61	13.9 ± 0.5	97^{+1}_{-1}	7.0
E4	121.8	267	2179	42	352	12	25	2.0 ± 1.6	150^{+1}_{-5}	0.4
E5	121.5	268	2183	41	319	18	37	6.1 ± 0.4	163^{+1}_{-1}	3.1
E6	120.8	270	2190	40	351	10	29	1.3 ± 0.6	188^{+1}_{-1}	−1.0
E7	120.3	271	2194	39	318	19	24	5.0 ± 0.7	149^{+1}_{-2}	2.4
F1	122.1	257	2143	53	191	22	31	8.0 ± 1.3	100^{+1}_{-9}	5.7
F2	122.3	258	2146	52	256	20	6	9.4 ± 0.6	102^{+1}_{-1}	4.8
F3	122.5	259	2150	51	223	4	17	4.9 ± 0.5	104^{+1}_{-1}	3.0
F4	122.6	260	2153	50	289	11	36	7.8 ± 0.6	148^{+1}_{-1}	6.1
F5	122.6	261	2157	48	256	17	37	3.5 ± 1.1	150^{+1}_{-7}	2.9
F6	122.6	262	2158	48	158	13	27	5.8 ± 0.4	130^{+1}_{-1}	1.7

[a]DOY is day of year (2005), Lat is latitude, Lon is longitude, $|B_{150}|$ is the magnetic field magnitude at 150 km [*Arkani-Hamed*, 2004], Inc is the angle between the field and the vertical, N_m is the peak density, z_m is the peak altitude, and TEC is total electron content. The 1σ uncertainty in total electron content is 5.6×10^9 cm^{-2} (section 5). All listed uncertainties are described in text.

[30] The two downlink radio signals at 8.4 GHz (X band) and 2.3 GHz (S band) follow different paths through the dense regions of the lower neutral atmosphere, which causes the assumptions underlying the differential Doppler technique to fail [*Pätzold et al.*, 2004, 2009]. Consequently, the derived electron density values are invalid below 70 km and we neglect densities below 70 km in this work. However, the electron density profiles shown in Figure 3 extend to the surface in order to illustrate that no grossly unusual behavior occurs at low altitudes.

[31] The uncertainties in the peak electron densities reported in Table 1 are the 1σ uncertainties introduced above. The asymmetric uncertainties in the corresponding peak altitudes reflect the vertical distances between the altitude of peak electron density and the two closest points above and below the peak at which the electron density profile first drops more than 1σ below the peak electron density. Table 1 also reports the total electron content, which we define as the integrated column density of electrons between 70 km and 250 km.

[32] The accuracy of the TEC values is affected more by systematic errors than random errors. To estimate these systematic errors, we considered the mean electron density between 500 km and 700 km altitude in each profile. These ranged from -10^3 cm^{-3} to $+10^3$ cm^{-3} with a root-mean-square of the 37 values of 310 cm^{-3}. Multiplying this by the 180 km distance over which our TEC values are calculated yields 5.6×10^9 cm^{-2}, which we adopt as the uncertainty in all the TEC values reported in Table 1. One profile, E6, has a negative TEC value, and its magnitude is almost twice the adopted uncertainty. This occurs because the systematic and random errors that affect the measured TEC value are sometimes appreciably greater than the typical errors we used to calculate the adopted uncertainty.

[33] All observations and models indicate that the nightside ionosphere of Mars varies irregularly with location (sections 2–4) and changes in nightside electron density over 260 km of horizontal distance must be accepted as highly likely. How, then, should radio occultation observations be used? Lacking a description of horizontal gradients in the ionosphere, no improvement in the data processing beyond the assumption of spherical symmetry is possible [*Kolosov et al.*, 1976]. In such instances, are the results obtained under the assumption of spherical symmetry meaningful? Given the currently weak state of knowledge concerning the nightside ionosphere, it is clear that small violations of spherical symmetry are tolerable, but large violations are not. Applying Occam's Razor, we initially accept the

derived density profiles as meaningful. If we later encounter major inconsistencies within the results or between the results and predictions from numerical models, we will revisit this choice.

6. Analysis of Observations and Insights From Models

6.1. Small Peak Plasma Densities

[34] Some profiles (B3, E4, and E6) are essentially devoid of plasma with peak electron densities of 3.3 ± 0.3, 2.0 ± 1.6, and $1.3 \pm 0.6 \times 10^3$ cm^{-3}, respectively.

[35] Assuming O_2^+ ions with a dissociative recombination coefficient of 2×10^{-7} cm^3 s^{-1}, the smallest of these values corresponds to a peak ionization rate of 0.3 cm^{-3} s^{-1}, which is comparable to the smallest values predicted by *Lillis et al.* [2011], but further work is needed to confirm this.

6.2. Meteoric Plasma Layers at 70–90 km

[36] Several profiles (A1, A2, B5, C1, C2, and C3) at SZA < 115° have a plasma layer at 70–90 km, the altitude at which dayside meteoric layers are observed [*Pätzold et al.*, 2005]. Although some of these layers are close to the 70 km altitude we have adopted as the lowest altitude at which these differential Doppler profiles are valid, we judge that these layers are authentic. Meteoric plasma, e.g., Mg$^+$, has a relatively long lifetime, on the order of 1 day. At the altitudes of interest here, atomic metal ions can easily persist into the dark ionosphere [*Whalley and Plane*, 2010; *Withers et al.*, 2008]. Peak densities of potential meteoric layers in the dark ionosphere are 5×10^3 cm^{-3} to 10^4 cm^{-3}, a range which approaches the dayside range of 1–2×10^4 cm^{-3} [*Withers et al.*, 2008].

[37] There are two reasons why it is reasonable that the range of peak densities in the dark ionosphere is somewhat smaller than the range of dayside densities. First, *Withers et al.* [2008] rejected the presence of potential meteoric layers with peak densities below 10^4 cm^{-3} on the basis of concerns about Mars Global Surveyor instrumental uncertainties. Second, the two dominant mechanisms producing metal ions, (1) photoionization of ablated neutral metal atoms and (2) production by charge exchange with the background ionosphere, are weaker in the dark ionosphere than on the dayside [*Pesnell and Grebowsky*, 2000; *Molina-Cuberos et al.*, 2003]. Theoretically, layers at 70–90 km in the dark ionosphere could be patchy plasma at higher altitudes some distance away from the occultation point (Figure 2). However, we do not favor this interpretation as the sharp vertical gradients on either side of these layers are difficult to produce with distributions of plasma that deviate substantially from spherical symmetry (section 3).

[38] Nevertheless, one alternative to the meteoric layer explanation is viable, as outlined in section 6.7.

6.3. Wide Plasma Layers Centered on 130 km

[39] Two profiles located at SZA < 105° (A4 and A5) display unusually wide layers of plasma with floors at 110 km and FWHM values of 60 km. These layers contain a weak local minimum located at about 130 km, suggesting that they could comprise the twilight M1 and M2 layers familiar from the dayside. Although this region is illuminated by sunlight, this explanation appears implausible,

as extrapolation based on trends from the dayside suggests that the predicted M2 altitude is above 180 km at SZA = 100° [*Hantsch and Bauer*, 1990; *Zhang et al.*, 1990] while the predicted M1 altitude is several tens of kilometers greater than 110 km (K. Fallows, personal communication, 2012). Further, the extrapolated peak densities are much smaller than those found in profiles A4 and A5. Instead, these may be a residual product of sunlight at the observed altitudes at a prior, smaller SZA that was subsequently transported horizontally to SZA = 104°. The photochemical lifetime of O_2^+ ions with a density of 10^4 cm^{-3} is about 10 min, so horizontal transport speeds of $\sim$2 km s^{-1} are required for this hypothesis to be plausible.

[40] The hypothesis above requires some explanation of why peak densities are so similar at 120 km and 150 km, given the significantly greater density of the M2 layer over that of the M1 layer. Perhaps plasma expands vertically as it is transported horizontally. An alternative explanation involves the increase in electron temperature and associated decrease in plasma loss rate with increasing altitude [*Hanson and Mantas*, 1988]. Perhaps the twilight M1 layer, whose altitude is higher than usual, occurs at a sufficiently high altitude for the electron temperature at the M1 layer to be significantly elevated above its usual value. In that instance, given the reduced plasma loss rate, the M1 layer density would be greater than expected based on extrapolation from the dayside.

6.4. Plasma Layers at 150 km Produced by Electron Precipitation

[41] Profiles D2, D4, and E5 exhibit a plasma layer centered on 150 km with peak densities of about 5×10^3 cm^{-3} unaccompanied by observable plasma at lower altitudes. We suggest that these layers correspond to the basic plasma layer produced by electron precipitation, as simulated by the numerical models summarized in section 4. The observed peak densities and altitudes are consistent with predictions from such models.

6.5. Large Plasma Densities at SZA > 120°

[42] Several profiles (E3, F1, and F2) at high solar zenith angles (120° < SZA < 123°) contain a broad, dense layer centered at 100 km altitude. These are among the largest peak densities observed beyond 100°, with values of 10^4 cm^{-3} and larger.

[43] If these low-altitude layers, whose peak electron densities are greater than those of the 150 km layers of section 6.4, are produced by electron precipitation, then unexpectedly large fluxes of electrons at few keV energies would be required.

[44] Although similar layers were produced by the electron precipitation model of *Fillingim et al.* [2010], we view those results with caution, as the input electron fluxes at high energies (>10 keV) for these simulations are too close to the instrumental background to be accepted as trustworthy (section 4).

6.6. Two Distinct Plasma Layers at 100 km and 160 km

[45] Two profiles at the largest solar zenith angles (F1 and F3) contain distinct plasma layers at both 100 km and 160 km. The two layers at 100 km are significantly more extended vertically than meteoric layers on the dayside and
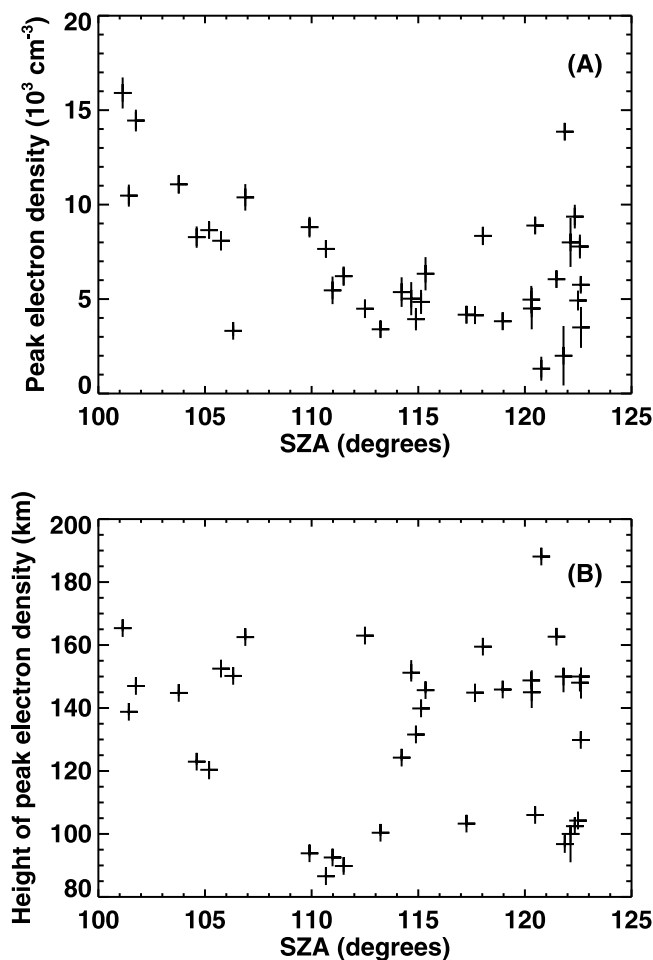
Figure 4. (a) Dependence of peak electron densities and (b) corresponding altitudes on solar zenith angle. Uncertainties of peak densities and altitudes are listed in Table 1. The length of the vertical arms of the crosses in Figures 4a and 4b indicate the uncertainties in peak electron density and peak altitude, although the uncertainties are in many cases smaller than the nominal size of the crosses. Note that an altitude of 120 km is illuminated by sunlight for SZA ≤ 105°.

the potential meteoric layers in the dark ionosphere discussed in section 6.2. Since these layers do not exhibit sharp vertical gradients, we cannot readily exclude the possibility that they are produced by plasma layers some horizontal distance away from the occultation point at a higher altitude (section 3).

6.7. Large Plasma Densities at or Below 100 km

[46] Several of the groups of profiles discussed above display large plasma densities at or below 100 km: these are challenging to explain by either electron precipitation or horizontal transport of dayside plasma. These profiles are: A1 and A2 (day of year 230); B5, C1, C2, and C3 (days of year 239–240); and E3, F1, F2, and F3 (days of year 256–259). Note that these subsets of profiles appear contemporaneously, which strongly suggests a temporally varying explanation.

[47] Although the 18 August to 1 October 2005 period studied in this paper was one of generally low solar activity,

it was punctuated by several significant events. Background counts in the MGS Electron Reflectometer and Odyssey Gamma Ray Spectrometer increased significantly multiple times during this interval with the increases persisting for periods of several days [*Morgan et al.*, 2006; *Espley et al.*, 2007], indicating the arrival of solar energetic particles (SEPs) at Mars; *Morgan et al.* [2006] also found that elevated densities of low-altitude plasma were present during these periods. During an SEP event, the flux of high-energy protons is elevated. This mechanism for plasma production differs from the common electron precipitation mechanism due to the particles involved, protons and heavier particles versus electrons.

[48] Studies of SEP events by *Withers* [2011] and *Sheel et al.* [2012] address the production of plasma densities at 70–100 km, as by *Sheel et al.* [2012, Figure 9]. Profiles B5, C1, C2, C3 (days of year 239–240) and E3, F1, F2, and F3 (days of year 256–259) were acquired during SEP events which may explain the presence of plasma at unusually low altitudes in these profiles [*Morgan et al.*, 2006, Figure 2].

[49] No SEP events occurred at Mars during the times when profiles A1 and A2 were acquired (day of year 230), which leaves meteoric plasma as the most likely explanation for the observed low-altitude layers. This possibility is not necessarily excluded by the absence of known meteor showers on this date, which corresponds to Ls = 269° [*Christou*, 2010], as the degree to which meteor showers associated with cometary orbits are responsible for meteoric layers on Mars has not been determined.

[50] The division of these nightside profiles into two sets, those acquired during SEP events and those not, distinguishes profiles A1 and A2 from profiles B5, C1, C2, and C3. A comparison of plasma densities at low altitudes does exactly the same. In profiles B5, C1, C2, and C3, plasma densities observed at 70–90 km exceed those at 110–170 km, unlike profiles A1 and A2.

6.8. General Trends

[51] Figure 4a illustrates the relationship between peak electron density and SZA. The spikes (section 5) in profiles E1, E4, F1, and F5 have been eliminated from our determination of these peak electron densities and peak altitudes. The peak density decreases with increasing solar zenith angle until SZA ≈ 115°, then increases again after SZA = 120°. The decrease is similar to that found in the occurrence rate of detectable ionospheric plasma by *Němec et al.* [2010], who report that the decreasing continued until SZA = 125°; it is unclear whether or not the difference between the 115° of this work and the 125° of *Němec et al.* [2010] is meaningful, given the statistical variations of the two data sets. Figure 4b shows the relationship between peak altitude and SZA.

[52] We identify three categories of profiles based on Figure 4. First, the peak altitudes of profiles with SZA < 108° are 120–170 km. The peak electron density in these profiles decreases with increasing SZA, from which we conclude that the source of plasma in these profiles is transport from the dayside. Second, the peak altitudes of some profiles with SZA > 108° are below 110 km. Many of these profiles were acquired during brief intervals when SEP events occurred at Mars, from which we conclude that the source of plasma in these profiles is SEP events. Third, the
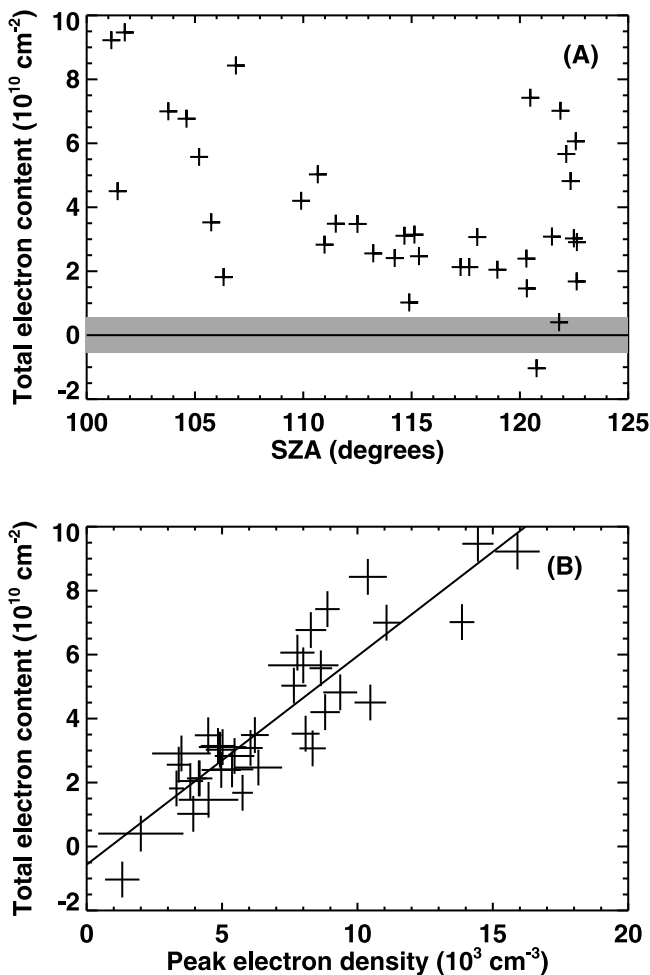
Figure 5. Dependence of total electron content on (a) solar zenith angle and (b) peak electron density. The 1σ uncertainty in total electron content is 5.6×10^9 cm^{-2}, as indicated by the shaded grey region in Figure 5a. Lengths of the horizontal and vertical arms of the crosses in Figure 5b indicate uncertainties in total electron content and peak electron density. The solid line in Figure 5b is a best fit to observations. Note that an altitude of 120 km is illuminated by sunlight for SZA $\leq 105°$.

peak altitudes of some profiles with SZA > 108° are 130–170 km. Based on comparisons with models, we conclude that the source of plasma in these profiles is electron precipitation. The 130–170 km range of peak altitudes is very similar to that found by *Zhang et al.* [1990]. The observation of low peak altitudes (90–100 km) at SZA > 108° in this work, but not by *Zhang et al.* [1990], can be explained if no SEP events perturbed Mars when the Viking data of *Zhang et al.* [1990] were collected.

[53] TEC values were calculated by direct integration of electron densities from 70 km to 250 km (Table 1). The 1σ uncertainty in TEC is 5.6×10^9 cm^{-2} (section 5). Figure 5a shows the relationship between TEC and SZA. Numerical values of nightside TEC and its decrease from SZA = 100° to SZA = 115° are consistent with results from MARSIS subsurface mode measurements [*Lillis et al.*, 2010 Figure 1]. Figure 5b shows an apparently linear relationship between

TEC and peak electron density. If an ensemble of data sets is generated using the uncertainties in both peak electron density and TEC, then the ensemble of correlation coefficients has a mean value of 0.86 and a standard deviation of 0.02, confirming a close correlation between peak electron density and TEC. *Lillis et al.* [2009] predicted TEC values of $3–4 \times 10^9$ cm^{-2} at weakly magnetized locations, similar to those observed here.

[54] Neglecting uncertainties on peak electron density and TEC, the best fit line relating peak electron density and TEC is TEC $= N_m \times 65$ km-5.7×10^9 cm^{-2}, where N_m is peak electron density. This is shown in Figure 5b. The length scale of 65 km can be interpreted as the slab thickness of the nightside ionosphere. A Monte Carlo study found the slab thickness to have a mean value of 63 km and a standard deviation of 4 km, and the intercept to have a mean value of -4.0×10^9 cm^{-2} and a standard deviation of 2.8×10^9 cm^{-2}. We do not consider the nonzero value of the intercept to be statistically significant and conclude that TEC is proportional to peak electron density. This observed slab thickness is similar to, but larger than, the 45–55 km predicted by *Lillis et al.* [2009].

[55] The observed correlation between peak electron density and TEC is impressive. If a single physical mechanism were responsible for maintaining the nightside ionosphere, then this high value for the correlation coefficient would not be too surprising. For instance, proportionality between TEC and peak electron density would be expected if both are proportional to some external factor, such as the intensity of solar irradiance or the flux of charged particles. Instead, some of the observations in Figure 5b come from profiles where the dominant process is transport of plasma from the dayside while others represent profiles where the dominant process is electron precipitation.

7. Conclusions

[56] Analysis of MaRS vertical electron density profiles shows that a range of morphologies is present in the dark ionosphere (SZA > 105°). Although the data processing algorithm assumes a spherically symmetric ionosphere, an assumption which is poorly satisfied by the dark ionosphere, the derived electron density profiles are useful nonetheless.

[57] Peak electron densities decrease with increasing solar zenith angle up to 115°, consistent with transport of dayside plasma as an important plasma source. At higher solar zenith angles, neither peak density nor peak altitude depend on solar zenith angle, suggesting that the transport of dayside plasma is no longer an important plasma source. Electron precipitation is likely to be the dominant source here under normal circumstances, leading to peak altitudes of 130–170 km. The energy spectrum and pitch angle distribution of these precipitating electrons depend on the magnetic environment, but due to the limitations set by the geographical distribution of this data set, we are unable to explore the influence of crustal field strength and direction on the dark ionosphere.

[58] During solar energetic particle events, low-altitude plasma densities are enhanced and peak altitudes can be much lower, 90 km, than usual. Two profiles (A1 and A2) at solar zenith angles of 101° may contain meteoric layers at ~80 km. Some regions of the dark ionosphere have such

low plasma densities that their peak electron density is $1.3 \pm 0.6 \times 10^3$ cm^{-3}. Total electron content is highly correlated with and nearly proportional to peak electron density, with a slab thickness of 65 km.

References

Arkani-Hamed, J. (2004), A coherent model of the crustal magnetic field of Mars, *J. Geophys. Res.*, 109, E09005, doi:10.1029/2004JE002265.

Bertaux, J.-L., F. Leblanc, O. Witasse, E. Quemerais, J. Lilensten, S. A. Stern, B. Sandel, and O. Korablev (2005), Discovery of an aurora on Mars, *Nature*, 435, 790–794, doi:10.1038/nature03603.

Christou, A. A. (2010), Annual meteor showers at Venus and Mars: Lessons from the Earth, *Mon. Not. R. Astron. Soc.*, 402, 2759–2770, doi:10.1111/j.1365-2966.2009.16097.x.

Duru, F., D. A. Gurnett, D. D. Morgan, J. D. Winningham, R. A. Frahm, and A. F. Nagy (2011), Nightside ionosphere of Mars studied with local electron densities: A general overview and electron density depressions, *J. Geophys. Res.*, 116, A10316, doi:10.1029/2011JA016835.

Espley, J. R., W. M. Farrell, D. A. Brain, D. D. Morgan, B. Cantor, J. J. Plaut, M. H. Acuña, and G. Picardi (2007), Absorption of MARSIS radar signals: Solar energetic particles and the daytime ionosphere, *Geophys. Res. Lett.*, 34, L09101, doi:10.1029/2006GL028829.

Fillingim, M. O., L. M. Peticolas, R. J. Lillis, D. A. Brain, J. S. Halekas, D. Lummerzheim, and S. W. Bougher (2010), Localized ionization patches in the nighttime ionosphere of Mars and their electrodynamic consequences, *Icarus*, 206, 112–119, doi:10.1016/j.icarus.2009.03.005.

Fjeldbo, G., A. J. Kliore, and V. R. Eshleman (1971), The neutral atmosphere of Venus as studied with the Mariner V radio occultation experiments, *Astron. J.*, 76, 123–140.

Fox, J. L., J. F. Brannon, and H. S. Porter (1993), Upper limits to the nightside ionosphere of Mars, *Geophys. Res. Lett.*, 20, 1339–1342, doi:10.1029/93GL01349.

Gurnett, D. A., et al. (2008), An overview of radar soundings of the martian ionosphere from the Mars Express spacecraft, *Adv. Space Res.*, 41, 1335–1346, doi:10.1016/j.asr.2007.01.062.

Haider, S. A., J. Kim, A. F. Nagy, C. N. Keller, M. I. Verigin, K. I. Gringauz, N. M. Shutte, K. Szego, and P. Kiraly (1992), Calculated ionization rates, ion densities, and airglow emission rates due to precipitating electrons in the nightside ionosphere of Mars, *J. Geophys. Res.*, 97, 10,637–10,641, doi:10.1029/92JA00317.

Hanson, W. B. and G. P. Mantas (1988), Viking electron temperature measurements: Evidence for a magnetic field in the Martian ionosphere, *J. Geophys. Res.*, 93, 7538–7544, doi:10.1029/JA093iA07p07538.

Hanson, W. B., S. Sanatani, and D. R. Zuccaro (1977), The Martian ionosphere as observed by the Viking retarding potential analyzers, *J. Geophys. Res.*, 82, 4351–4363, doi:10.1029/JS082i028p04351.

Hantsch, M. H., and S. J. Bauer (1990), Solar control of the Mars ionosphere, *Planet. Space Sci.*, 38, 539–542.

Hinson, D. P., R. A. Simpson, J. D. Twicken, G. L. Tyler, and F. M. Flasar (1999), Initial results from radio occultation measurements with Mars Global Surveyor, *J. Geophys. Res.*, 104, 26,997–27,012, doi:10.1029/1999JE001069. (Correction to "Initial results from radio occultation measurements with Mars Global Surveyor" by D. P. Hinson et al., *J. Geophys. Res.*, 105, 1717, doi:10.1029/1999JE900045, 2000.)

Kliore, A. J. (1992), Radio occultation observations of the ionospheres of Mars and Venus, in *Venus and Mars: Atmospheres, Ionospheres, and Solar Wind Interactions*, Geophys. Monogr. Ser., vol. 66, edited by J. G. Luhmann, M. Tatrallyay, and R. O. Pepin, pp. 265–276, AGU, Washington, D. C., doi:10.1029/GM066p0265.

Kliore, A. J., D. L. Cain, G. Fjeldbo, B. L. Seidel, M. J. Sykes, and S. I. Rasool (1972), The atmosphere of Mars from Mariner 9 radio occultation measurements, *Icarus*, 17, 484–516.

Kliore, A. J., G. Fjeldbo, B. L. Seidel, M. J. Sykes, and P. M. Woiceshyn (1973), S band radio occultation measurements of the atmosphere and topography of Mars with Mariner 9: Extended Mission coverage of polar and intermediate latitudes, *J. Geophys. Res.*, 78, 4331–4351, doi:10.1029/JB078i020p04331.

Kolosov, M. A., V. M. Ivanov, D. S. Lukin, and I. G. Spiridonov (1976), Radio occultation of the Martian ionosphere taking into account horizontal gradients of electron density, in *Space Research XVI*, pp. 1013–1017, Akademie-Verlag, Berlin.

Lillis, R. J., M. O. Fillingim, L. M. Peticolas, D. A. Brain, R. P. Lin, and S. W. Bougher (2009), Nightside ionosphere of Mars: Modeling the effects of crustal magnetic fields and electron pitch angle distributions on electron impact ionization, *J. Geophys. Res.*, 114, E11009, doi:10.1029/2009JE003379.

Lillis, R. J., D. A. Brain, S. L. England, P. Withers, M. O. Fillingim, and A. Safaeinili (2010), Total electron content in the Mars ionosphere: Temporal studies and dependence on solar EUV flux, *J. Geophys. Res.*, 115, A11314, doi:10.1029/2010JA015698.

Lillis, R. J., M. O. Fillingim, and D. A. Brain (2011), Three-dimensional structure of the Martian nightside ionosphere: Predicted rates of impact ionization from Mars Global Surveyor magnetometer and electron reflectometer measurements of precipitating electrons, *J. Geophys. Res.*, 116, A12317, doi:10.1029/2011JA016982.

Lindal, G. F., H. B. Hotz, D. N. Sweetnam, Z. Shippony, J. P. Brenkle, G. V. Hartsell, R. T. Spear, and W. H. Michael Jr. (1979), Viking radio occultation measurements of the atmosphere and topography of Mars: Data acquired during 1 Martian year of tracking, *J. Geophys. Res.*, 84, 8443–8456, doi:10.1029/JB084iB14p08443.

Lipa, B., and G. L. Tyler (1979), Statistical and computational uncertainties in atmospheric profiles from radio occultation: Mariner 10 at Venus, *Icarus*, 39, 192–208, doi:10.1016/0019-1035(79)90163-5.

Lollo, A., P. Withers, K. Fallows, Z. Girazian, M. Matta, and P. C. Chamberlin (2012), Numerical simulations of the ionosphere of Mars during a solar flare, *J. Geophys. Res.*, 117, A05314, doi:10.1029/2011JA017399.

Mendillo, M., S. Smith, J. Wroten, H. Rishbeth, and D. Hinson (2003), Simultaneous ionospheric variability on Earth and Mars, *J. Geophys. Res.*, 108(A12), 1432, doi:10.1029/2003JA009961.

Mendillo, M., A. Lollo, P. Withers, M. Matta, M. Pätzold, and S. Tellmann (2011), Modeling Mars' ionosphere with constraints from same-day observations by Mars Global Surveyor and Mars Express, *J. Geophys. Res.*, 116, A11303, doi:10.1029/2011JA016865.

Molina-Cuberos, G. J., O. Witasse, J.-P. Lebreton, R. Rodrigo, and J. J. López-Moreno (2003), Meteoric ions in the atmosphere of Mars, *Planet. Space Sci.*, 51, 239–249.

Morgan, D. D., D. A. Gurnett, D. L. Kirchner, R. L. Huff, D. A. Brain, W. V. Boynton, M. H. Acuña, J. J. Plaut, and G. Picardi (2006), Solar control of radar wave absorption by the Martian ionosphere, *Geophys. Res. Lett.*, 33, L13202, doi:10.1029/2006GL026637.

Moroz, V. I. (1976), The atmosphere of Mars, *Space Sci. Rev.*, 19, 763–843.

Němec, F., D. D. Morgan, D. A. Gurnett, and F. Duru (2010), Nightside ionosphere of Mars: Radar soundings by the Mars Express spacecraft, *J. Geophys. Res.*, 115, E12009, doi:10.1029/2010JE003663.

Němec, F., D. D. Morgan, D. A. Gurnett, and D. A. Brain (2011), Areas of enhanced ionization in the deep nightside ionosphere of Mars, *J. Geophys. Res.*, 116, E06006, doi:10.1029/2011JE003804.

Pätzold, M., et al. (2004), MaRS: Mars Express Orbiter Radio Science, *Eur. Space Agency Spec. Publ.*, ESA SP-1240, 141–163. [Available at http://sci.esa.int/science-e/www/object/index.cfm?fobjectid=34885.]

Pätzold, M., S. Tellmann, B. Häusler, D. Hinson, R. Schaa, and G. L. Tyler (2005), A sporadic third layer in the ionosphere of Mars, *Science*, 310, 837–839, doi:10.1126/science.1117755.

Pätzold, M., et al. (2009), MaRS: Mars Express Radio Science Experiment, *Eur. Space Agency Spec. Publ.*, ESA SP-1291, 217–245. [Available at http://sci.esa.int/science-e/www/object/index.cfm?fobjectid=47218.]

Pesnell, W. D., and J. Grebowsky (2000), Meteoric magnesium ions in the Martian atmosphere, *J. Geophys. Res.*, 105, 1695–1708, doi:10.1029/1999JE001115.

Safaeinili, A., W. Kofman, J. Mouginot, Y. Gim, A. Herique, A. B. Ivanov, J. J. Plaut, and G. Picardi (2007), Estimation of the total electron content of the martian ionosphere using radar sounder surface echoes, *Geophys. Res. Lett.*, 34, L23204, doi:10.1029/2007GL032154.

Savich, N. A., and V. A. Samovol (1976), The night time ionosphere of Mars from Mars 4 and Mars 5 dual-frequency radio occultation measurements, in *Space Research XVI*, pp. 1009–1011, Akademie-Verlag, Berlin.

Schunk, R. W., and A. F. Nagy (2009), *Ionospheres*, 2nd ed., Cambridge Univ. Press, New York.

Sheel, V., S. A. Haider, P. Withers, K. Kozarev, I. Jun, S. Kang, G. Gronoff, and C. Simon Wedlund (2012), Numerical simulation of the effects of a

solar energetic particle event on the ionosphere of Mars, *J. Geophys. Res.*, *117*, A05312, doi:10.1029/2011JA017455.

Vasil'ev, M. B., et al. (1975), Preliminary results of the two-frequency radio-transillumination of the Martian ionosphere by means of the "Mars" automatic interplanetary stations in 1974, *Cosmic Res.*, *13*, 41–45.

Whalley, C. L., and J. M. C. Plane (2010), Meteoric ion layers in the Martian atmosphere, *Faraday Discussions*, *147*, 349–368, doi:10.1039/c003726e.

Withers, P. (2009), A review of observed variability in the dayside ionosphere of Mars, *Adv. Space Res.*, *44*, 277–307, doi:10.1016/j.asr.2009.04.027.

Withers, P. (2011), Attenuation of radio signals by the ionosphere of Mars: Theoretical development and application to MARSIS observations, *Radio Sci.*, *46*, RS2004, doi:10.1029/2010RS004450.

Withers, P., M. Mendillo, D. P. Hinson, and K. Cahoy (2008), Physical characteristics and occurrence rates of meteoric plasma layers detected in the Martian ionosphere by the Mars Global Surveyor Radio Science Experiment, *J. Geophys. Res.*, *113*, A12314, doi:10.1029/2008JA013636.

Zhang, M. H. G., J. G. Luhmann, and A. J. Kliore (1990), An observational study of the nightside ionospheres of Mars and Venus with radio occultation methods, *J. Geophys. Res.*, *95*, 17,095–17,102, doi:10.1029/JA095iA10p17095.